Technical Report

High-energy X-ray Study of Dislocation Dynamics Under Torsion in SUS304 Steel

Satoshi SUGANO* Mitsuharu YONEMURA

Abstract

To elucidate the dislocation behavior and deformation-induced martensitic transformation during torsional deformation of SUS304 steel, in situ high-energy X-ray diffraction experiments were conducted. Line profile analysis enabled quantitative evaluation of the evolution of dislocation density and diffraction intensity during deformation, which was further correlated with microstructural characterization by electron microscopy. The results revealed distinct variations in dislocation density and demonstrated that ε phase formation is suppressed under torsional loading compared with uniaxial deformation. These findings advance the understanding of deformation mechanisms in austenitic steels and provide a fundamental basis for the assessment of mechanical properties and the development of material design strategies.

1. Introduction

Steel is one of the most widely used structural materials in automotive and construction sectors. Owing to its advantageous material properties, cost-effectiveness, and recyclability, it holds a substantially larger market share than other structural materials. Structural materials are required to prevent damage caused by loads and impacts and thereby ensure human safety; therefore, improving mechanical properties such as strength, ductility, and toughness remains a central challenge.[1] In addition, environmental performance has become increasingly important from the perspective of energy conservation and CO_2 emission reduction. In automotive applications, weight reduction is a key factor, prompting significant advances in the development of high-strength steels and associated processing technologies.[2] In the infrastructure sector, ensuring long-term durability is also essential. To meet these diverse requirements, it is indispensable to understand deformation and fracture behavior under conditions that closely resemble actual service conditions, particularly from the perspective of microstructural evolution.

Under practical service conditions, steel components experience not only uniaxial tension and compression but also complex stress states such as torsion and bending. For example, driveline components and seatbelt anchorage systems in automobiles are subjected to cyclic torque, whereas structural steels in buildings experience combined loading from earthquakes and fluctuating service loads.[3] Consequently, understanding shear deformation is particularly important. *In situ* observation of torsional deformation provides an effective approach for clearly capturing microstructural evolution during deformation. Torsion introduces a rotationally symmetric shear stress field, offering excellent experimental controllability. Moreover, bar-shaped specimens exhibit a continuous radial strain distribution, enabling the simultaneous evaluation of multiple strain levels within a single specimen. When combined with transmission electron microscopy (TEM) and transmission Kikuchi diffraction (TKD) in a scanning electron microscope (SEM), multiscale and multimodal analyses of dislocation structures, phase transformations, and local strains can be achieved. In addition, the multiaxial stress state generated by torsional deformation enables the observation of dislocation density distributions and localized martensitic transformation behavior that are difficult to detect under conventional uniaxial tensile deformation.

Recent advances in *in situ* techniques using two-dimensional (2D) pixel detectors[4] have significantly improved observation capabilities. As a result, synchrotron X-ray diffraction (XRD) methods have progressed considerably and are now widely applied to the quantitative evaluation of stress and strain states, as well as to the analysis of phase transformations and lattice defect behavior. Our group has also contributed to the development of *in situ* observation techniques under various deformation and thermal-history conditions, including hot compression[5, 6] and ultrafast heating and cooling using X-ray free-electron lasers.[7] XRD enables the simultane-

* Materials Characterization Research Lab., Advanced Technology Research Laboratories
1-8 Fuso-Cho, Amagasaki City, Hyogo Pref. 660-0891

ous quantitative evaluation of microstructural changes, such as variations in dislocation density and phase transformations, making it particularly suitable for torsional deformation studies. Although *in situ* XRD has been applied to high-pressure torsion (HPT),[8] its application to conventional torsional deformation has not yet been reported.

In the present study, *in situ* observations during torsional deformation were conducted using high-energy XRD on metastable austenitic stainless steel SUS304, which exhibits deformation-induced martensitic transformation at room temperature.[9] The evolution of dislocation density and martensitic transformation during deformation was quantitatively evaluated. Furthermore, TEM and SEM-based TKD analyses of interrupted specimens were performed to verify the validity and correlation of the *in situ* observations.

2. Experiments

2.1 Test specimens

Table 1 shows the chemical composition of the test material. SUS304 steel possesses metastable austenite (γ) phase at room temperature and is known to undergo deformation-induced phase transformation during cold working. The specimens used for *in situ* XRD observation were machined from commercially available cold-finished SUS304 steel bars conforming to JIS G 4318:2016. The specimen geometry was designed based on a conventional torsion test specimen shape. In order to ensure sufficient X-ray transmission, the torsional deformation region was designed with a diameter of 1.0 mm and a gauge length of 2.0 mm.

TEM and TKD specimens for microstructural observation were extracted from torsionspecimens using a focused ion beam (FIB) system. The specimens consist of six conditions: an undeformed specimen (①), a specimen deformed until fracture (⑥), and four interrupted specimens deformed to twist angles of 72° (②), 552° (③), 1 032° (④), and 1395° (⑤), under the same conditions as *in situ* XRD observation. In this study, the average plastic shear strain $\bar{\gamma}$ within the X-ray irradiation region is defined by Equation (1).

$$\bar{\gamma} = \frac{1}{S}\int_0^R \frac{4r^2\theta\phi_{(r)}}{L}\,dr \qquad (1)$$

where r is radius of the cylindrical cross-section, R is maximum radius of the deformed region, θ is twist angle, L is extent of the deformed region, $\phi_{(r)}$ is weighting function for the X-ray irradiation region, S is the X-ray irradiation region.

Assuming the cylindrical specimen twists uniformly along its longitudinal direction, the shear strain is assumed to be distributed proportionally along the radial direction. Under this assumption, $\bar{\gamma}$ represents the area-weighted average shear strain within the X-ray irradiation region, and it was used as an indicator of the deformation level of each specimen. The specimens ① to ⑥ correspond to $\bar{\gamma}$ = 0, 0.15, 1.2, 2.2, 2.9, and 3.3, respectively. For all specimens, those used for microstructural observation were extracted from the circular cross-section at the center of the deformed region. However, since the fractured specimen (⑥) fractured outside the central region, the fracture surface was first mechanically polished to obtain a flat surface, and then the specimen was extracted from the center of the cross-section.

Table 1 Chemical composition of the SUS304 steel

(mass%)

C	Si	Mn	P	S	Ni	Cr	Fe
0.08	0.27	1.35	0.035	0.023	8.17	18.33	Bal.

2.2 Measurement

In situ X-ray diffraction measurements were performed at the second hutch of the SPring-8 public beamline BL13XU (**Fig. 1**). Considering spatial resolution and X-ray penetration, monochromatic high-energy X-rays (70 keV) were used, with a beam size of 0.2 × 0.5 mm. During continuous torsional deformation at a rate of 2°/s, diffraction data were collected in transmission geometry. The diffracted X-rays were detected using an energy-threshold CdTe 2D detector developed by the Japan Synchrotron Radiation Research Institute (JASRI).[10] The detector had 191 × 201 effective pixels with a pixel size of 200 μm, and the camera length was 400 mm. The 2θ measurement range was approximately 4° to 15°, with low- and high-angle regions measured separately. The 2D diffraction images obtained with an exposure time of 0.1 s were integrated along the Debye-Scherrer ring direction, converted into line profiles for subsequent analysis. In addition, the temperature rise due to deformation-induced heating under torsion was measured using a low-temperature pyrometer. The torsional load applied to the specimen was controlled by a stepping motor and controller, and the deformation start pulse was used as a trigger signal to synchronize with the detector. This setup enabled simultaneous data acquisition from the onset of deformation.

The diffraction profiles for each set of lattice planes were fitted using a pseudo-Voigt function, and the full width at half maximum (FWHM) of the diffraction peaks corresponding to the {111}–{422} planes of the γ phase was extracted and used to evaluate dislocation density. To eliminate the influence of instrumental broadening, the experimental profiles were deconvoluted using the diffraction profile of a standard specimen, LaB_6 (NIST SRM 660c), to correct for the instrumental broadening. Furthermore, to evaluate the evolution of deformation-induced martensite (α'), the integral intensity ratio (A) of α' martensite, as defined in Equation (2), was calculated from the integral intensities of the diffraction peaks corresponding to the {111}, {200}, and {220} planes of the γ phase and the {110}, {200}, and {211} planes of the α' martensite. This ratio served as an approximate indicator of the α' martensite volume fraction.

$$A=(I_{\alpha'110}+I_{\alpha'200}+I_{\alpha'211})/(I_{\gamma111}+I_{\gamma200}+I_{\gamma220}+I_{\alpha'110}+I_{\alpha'200}+I_{\alpha'211}) \qquad (2)$$

TEM observations were performed using a JEOL JEM-2100 PLUS. Bright-field images were acquired at an acceleration voltage of 200 kV, and the macroscopic average dislocation density evaluated by XRD was compared with the observed microstructure. In addition, TKD measurements were performed using a FEI Helios system to obtain obtain crystallographic orientation and phase information of the microstructure. The measurement area was 5.5 μm × 6 μm with a step size of 50 nm, and crystallographic orientation maps

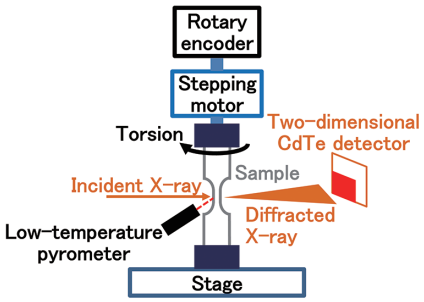

Fig. 1 Schematic illustration of *in-situ* measurement during tortional deformation

and phase maps were acquired using a hexagonal grid.

2.3 X-ray line profile analysis

In metals subjected to plastic deformation, lattice strain is introduced by dislocations, resulting in domain structures such as low-angle grain boundaries and dislocation cells. These features manifest in XRD patterns as peak broadening and profile changes that depend on crystallographic indices. X-ray line profile analysis (XLPA) is a technique used to separate and quantitatively evaluate dislocation density and stacking fault probability from diffraction peak profiles. Classical approaches include the Williamson-Hall (WH) method and the Warren-Averbach (WA) method, with recent developments incorporating elastic anisotropy into these analyses. In particular, the theory proposed by Ungár et al. provides an accurate description of diffraction line profiles based on the relationship between anisotropic strain associated with crystallographic orientation and the strain fields of dislocations.[11] By combining the modified WH (mWH) method and modified WA (mWA) method based on this theory, dislocation density and characteristics, including strain-field magnitude and the character of dislocations, can be quantitatively evaluated.

The mWH equation is shown in Equation (3).

$$\Delta K = \frac{0.9}{D} + \left(\frac{\pi M^2 b^2}{2}\right)^{\frac{1}{2}} \cdot \rho^{\frac{1}{2}} K C^{\frac{1}{2}} + O(K^2 C) \quad (3)$$

Here, M and O are constants related to dislocation arrangement, b is the Burgers vector, ρ is the dislocation density, and C is the mean contrast factor. The mWA equation is expressed by Equation (4), where R_e represents the effective dislocation interaction distance.

$$lnA(L) = lnA^s(L) - \rho \cdot \frac{\pi b^2}{2} \cdot L^2 \cdot ln\left(\frac{R_e}{L}\right) \cdot (K^2 C) + Q(K^4 C^2) \quad (4)$$

Here, L is the Fourier length, $A(L)$ is the Fourier coefficient, $A^s(L)$ is the size-related Fourier coefficient, and Q denotes higher-order terms.

3. Results and Discussion

3.1 High-energy XRD *in-situ* observation

Figure 2 shows a representative example of the time-dependent change in XRD intensity during the torsional deformation. Before deformation, the specimen consisted of a single γ phase with a face-centered cubic (FCC) lattice. In the early stage of deformation, only diffraction peaks corresponding to the {111}–{220} planes of the γ phase were observed. As deformation progressed, plastic strain accumulated, resulting in broadening of the FWHM of these diffraction peaks. At the same time, diffraction peaks corresponding to the {110}–{211} planes of α' martensite with a body-centered cubic (BCC) lattice appeared, and their intensities increased with increasing deformation. In contrast, the ε phase with a hexagonal close-packed (HCP) lattice, previously observed under uniaxial stress in *in situ* tensile[12] and cold compression experiments[13] on SUS304 steel, was not detected under the multiaxial stress conditions of torsional deformation in the present study. This result suggests that the stress state significantly influences the phase transformation behavior. The formation of the ε phase is known to be strongly affected by the stacking fault energy (SFE) and deformation temperature.[14] However, both the cold compression test, where the ε phase was observed, and the present torsional deformation experiment employed commercially available SUS304 steel with chemical composition conforming to JIS standards, and therefore no significant difference in SFE is expected. Furthermore, the deformation rate in the present experiment was relatively low, and the temperature rise caused by deformation-induced heating under torsion—measured using a low-temperature pyrometer—was small (a maximum temperature rise of approximately 50°C). Accordingly, the influence of deformation temperature is considered to be limited.

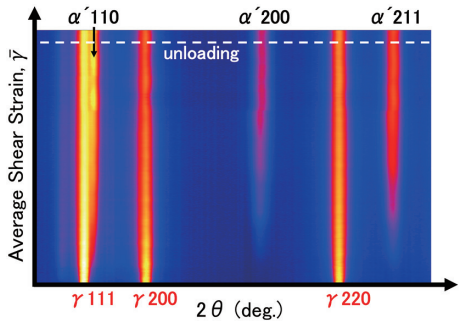

Fig. 2 Line profile changes associated with torsional deformation

From these considerations, the suppression of ε phase formation in the present study is attributed primarily to the difference in loading condition, namely, the contrast between uniaxial stress (tension or compression) and multiaxial stress (torsion). A similar suppression of the ε phase has also been reported in previous studies on HPT processing.[15] This suggests that the phenomenon is a common characteristic of torsional deformation in SUS304 steel, regardless of the presence or absence of hydrostatic pressure. Considering this phenomenon from the viewpoint of slip system activity and stacking fault formation, plastic deformation in FCC metals under uniaxial stresses such as tension or compression generally begins with preferential activation of the slip system with the maximum Schmid factor. As deformation proceeds, crystallographic rotation occurs due to primary slip, aligning the slip direction with the principal stress direction and subsequently activating additional slip systems (secondary slip systems). During the stage dominated by primary slip, deformation tends to concentrate on specific crystallographic planes, promoting the introduction of stacking faults and thereby facilitating ε phase formation. In contrast, under multiaxial stress conditions such as torsion, deformation is not confined to a single crystallographic plane; instead, multiple slip systems are activated simultaneously. As a result, the relative contribution of in-plane slip is reduced, suppressing the introduction of stacking faults and consequently inhibiting ε phase formation.

Figure 3 shows the change in the integral intensity ratio of α' martensite obtained during torsional deformation. The black dashed line ($\bar{\gamma}$ = 3.3) in the figure corresponds to the point at which the increase in the integral intensity ratio decreased, indicating the average shear strain $\bar{\gamma}$ at which stress relaxation associated with specimen fracture is presumed to occur. The diffraction data were obtained by integrating the 2D diffraction patterns along the Debye-Scherrer ring direction and calculating the integral intensity ratio from the resulting line profiles. This ratio can be interpreted as approximately corresponding to the volume fraction of each phase. The dashed line in the figure represents a linear approximation of the experimental data. The results show that the integral intensity ratio of α' martensite increases almost linearly with increasing torsional deformation and reaches approximately 0.33 at $\bar{\gamma}$ = 3.0. Subsequently, just before fracture, the ratio increases rapidly, indicating accelerated formation of α' martensite likely due to localized stress concentration near the crack tip. This phenomenon is considered to

be caused by the proximity of the X-ray irradiation region to the crack initiation site and the local promotion of phase transformation due to stress concentration. Deformation-induced α' martensite is known to preferentially form in regions of stress concentration. In the present specimen, localized reduction of the cross-sectional area near the fracture region reduced torque and concentrated stress at the crack tip. As a result, it is likely that phase transformation in this region proceeded rapidly.

Figure 4 shows the change in dislocation density within the γ phase obtained during torsional deformation. The red dashed line represents the variation in dislocation density approximated from the measured values. The black dashed lines indicate the strains $\bar{\gamma}$ = 0.3 and $\bar{\gamma}$ = 2.4, where significant increases in dislocation density were observed. At $\bar{\gamma}$ = 3.1, a decrease in dislocation density was observed, which is presumed to result from stress relaxation associated with crack initiation. The XLPA indicated that almost no α' martensite was generated in the initial stage of deformation. Although the specimens were machined from commercially available cold-finished bars, the influence of the machining history is therefore considered to be limited. Consequently, the initial dislocation density (approximately $7 \times 10^{13}/m^2$) likely originated from prior hot working applied to the γ single-phase region during bar manufacturing.

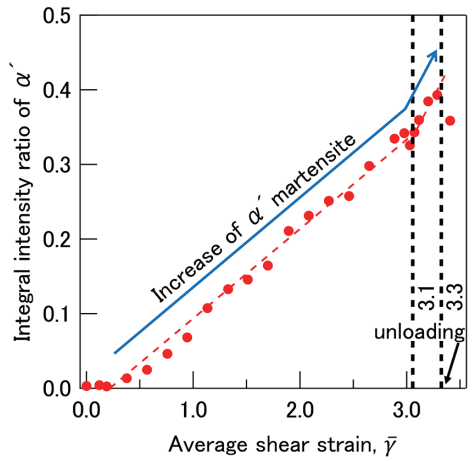

Fig. 3 Change in the integrated intensity of the α' martensite during torsional deformation

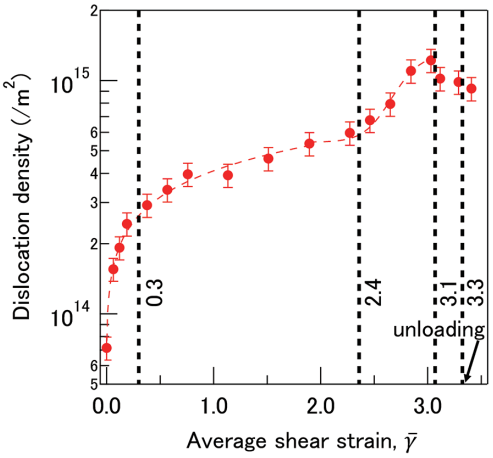

Fig. 4 Change in the dislocation density of the γ phase during torsional deformation

Immediately after the onset of deformation, the dislocation density increased rapidly in the low strain region ($\bar{\gamma} \leq 0.3$) due to work hardening and subsequently increased more gradually. This behavior is consistent with typical dislocation introduction mechanisms associated with cold working and indicates plastic deformation is primarily accommodated by dislocation motion. In the high strain region, however, the increase in dislocation density temporarily stagnated and then increased rapidly again after exceeding a critical strain ($\bar{\gamma}$ = 2.4). Such a two-stage evolution of dislocation density may be associated with activation of secondary slip systems, localized microstructural changes, or interactions with deformation-induced α' martensitic transformation. Further investigation is required to clarify the detailed mechanism.

3.2 Microstructural observation by TEM/TKD

Figure 5 shows bright-field TEM images of each specimen after interrupted torsional deformation (the numbers correspond to the specimen numbers defined in Section 2.1). Specimen ① ($\bar{\gamma}$ = 0) exhibited a microstructure originating from the manufacturing process, and no characteristic dislocation structures or deformation twins were observed. Specimen ② ($\bar{\gamma}$ = 0.15) showed contrast attributable to stacking faults in some areas. In specimen ③ ($\bar{\gamma}$ = 1.2), microstructures identified as deformation twins with widths of approximately 50 nm were observed within linear structures wider than 1 μm that are identified as annealing twins. Although XRD suggested an increase in dislocation density, no clear dislocation cell structures were observed, and dislocation tangles were dominant. In specimen ④ ($\bar{\gamma}$ = 2.2), clear dislocation cell structures were observed for the first time together with the development of deformation twins. This observation is consistent with the rapid increase in dislocation den-

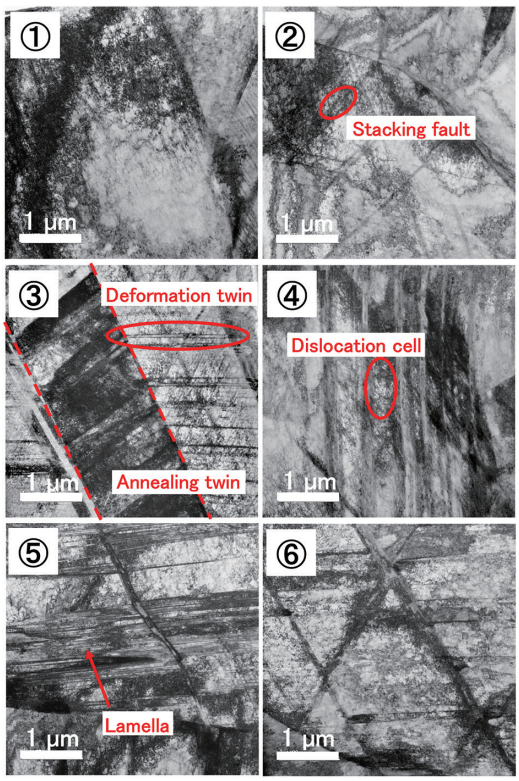

Fig. 5 Bright-field TEM images of specimens interrupted during torsional deformation

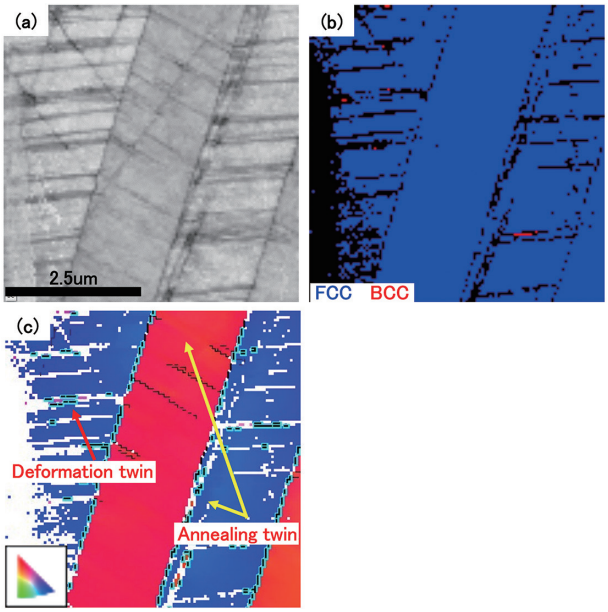

Fig. 6 TKD maps of the specimen interrupted at $\bar{\gamma}$=1.2 of tortional deformation
(a) Band contrast map, (b) Phase map and (c) IPF map

sity observed by XRD analysis. In specimen ⑤ ($\bar{\gamma}$ = 2.9), even finer lamellar microstructures appeared. Although X-ray analysis suggested a decrease in dislocation density after fracture, TEM observations did not reveal a clear reduction in dislocations, indicating that a high dislocation density remained.

Furthermore, detailed microstructural analysis of specimen ③ ($\bar{\gamma}$ = 1.2) was performed using TKD. **Figure 6** shows the band contrast map (a), crystal phase map (b), and inverse pole figure (IPF) map (c), which visualize crystallographic regularity and defect distribution. The same observation region as that in the TEM analysis was examined, although the observation plane is inverted. The broad linear boundaries extending diagonally were identified as annealing twins having a rotation relationship of 60±10° about a common ⟨111⟩ rotation axis. In contrast, the fine linear boundaries intersecting these were also identified as twin boundaries and were therefore interpreted as deformation twins. In addition, a small amount of BCC phase was detected near the twin boundaries, which was identified as deformation-induced α' martensite. This observation is consistent with previous studies.[14] The HCP ε phase was not detected in this measurement either. The black regions observed in the phase map are attributed to indexing errors caused by strain-induced distortion of the diffraction pattern or phase overlap.

These results demonstrate that dislocation density increases in two stages during torsional deformation, accompanied by the development of deformation twins and localized formation of deformation-induced α' martensite. Although these microstructural changes promote work hardening and contribute to strength enhancement, excessive dislocation accumulation and phase transformations may lead to stress concentration, thereby reducing workability and increasing the risk of crack initiation. In particular, rapid formation of α' martensite may result in a reduction in ductility. These findings provide fundamental guidelines for optimizing the design and processing conditions of high-strength steel materials with excellent workability.

4. Conclusion

In this study, *in situ* observations of torsional deformation in SUS304 steel were conducted using high-energy 2D X-ray diffraction, enabling clear evaluation of deformation-induced phase transformations and dislocation density evolution. The obtained results were consistent with microstructural observations of interrupted specimens using TEM and TKD, quantitatively demonstrating differences in dislocation introduction and phase transformation behavior between uniaxial (tensile and compressive) deformation and torsional deformation. This study is significant in that it visualizes shear deformation of high practical importance through *in situ* observation. The results deepen the understanding of deformation behavior in steel materials and provide insights useful for accurate prediction of product properties and development and optimization of structural materials. Future work will focus on systematic investigation of microstructural evolution at the center and surface of torsion specimens as well as collection of torsion fatigue test data. These studies are expected to contribute to practical material development, including the improvement of structural material performance and design accuracy, in response to the demands of carbon neutrality and digital transformation in manufacturing.

References

1) NEDO Technology Strategy Center Report: TSC Foresight. 25, Structural Materials Field. (2018)
2) Uenishi, A.: Nippon Seitetsu Giho. (412), 8 (2019)
3) Hanya, K. et al.: Nippon Seitetsu Giho. (420), 117 (2023)
4) Yonemura, M. et al.: Mater. Trans. 47, 2292 (2006)
5) Yonemura, M. et al.: Metal. Mater. Trans. A 56, 1193 (2025)
6) Sugano, S. et al.: SPring-8/SACLA Research Report. 12 (1), 45 (2024)
7) Yonemura, M. et al.: Sci. Rep. 9, 11241 (2019)
8) Kerber, M. B. et al.: Adv. Eng. Mater. 23, 2100159 (2021)
9) Sugano, S. et al.: SPring-8/SACLA Research Report. 13 (5), 351 (2025)
10) Toyokawa, H., Hyodo, K.: Journal of the Japanese Society for Synchrotron Radiation Research. 22, 256 (2009)
11) Ungár, T., Borbely, A.: Appl. Phys. Lett. 69 (21), 3173 (1996)
12) Hatano, M. et al.: Philos. Mag. Lett. 96 (6), 220 (2016)
13) Yonemura, M. et al.: SPring-8/SACLA Research Report. 10 (2), 215 (2022)
14) Das, A., Tarafder, S.: Inter. J. Plastic. 25, 2222 (2009)
15) Haraguchi, D. et al.: Proceedings of the 155th Autumn Annual Meeting of the Japan Institute of Metals and Materials. Aichi, 2014-9, The Japan Institute of Metals and Materials

Satoshi SUGANO
Materials Characterization Research Lab.
Advanced Technology Research Laboratories
1-8 Fuso-Cho, Amagasaki City, Hyogo Pref. 660-0891

Mitsuharu YONEMURA
Dr. Eng., Leading Researcher
Advanced Technology Research Laboratories